AUGUST 15 2019

Broadband acoustic scattering from oblate hydrocarbon droplets

Scott Loranger; Geir Pedersen; Thomas C. Weber

J. Acoust. Soc. Am. 146, 1176–1188 (2019)
https://doi.org/10.1121/1.5121699

Broadband acoustic scattering from oblate hydrocarbon droplets

Scott Loranger,[1,a)] Geir Pedersen,[2] and Thomas C. Weber[3]
[1]*Department of Earth Sciences, University of New Hampshire, 105 Main Street, Durham, New Hampshire 03824, USA*
[2]*Norwegian Research Centre, P.O. Box 6031, Bergen 5892, Norway*
[3]*Department of Mechanical Engineering, University of New Hampshire, 105 Main Street, Durham, New Hampshire 03824, USA*

(Received 24 October 2018; revised 24 July 2019; accepted 24 July 2019; published online 15 August 2019)

Improved *in situ* quantification of oil in the marine environment is critical for informing models of fate and transport and evaluating the resiliency of marine communities to oil spills. Broadband acoustic backscatter has been used to quantify a variety of targets in the water column; from fish and planktonic organisms to gas bubbles and oceanic microstructure, and shows promise for use in quantifying oil droplets. Quantifying water column targets with broadband acoustic backscatter relies on accurate models of a target's frequency dependent target strength (TS), a function of the target's acoustic impedance, shape, and size. Previous acoustic quantification of oil droplets has assumed that droplets were spheres. In this study, broadband (100.5–422 kHz) acoustic backscatter from individual oil droplets was measured, and the frequency dependent TS compared to a model of acoustic scattering from fluid spheres and two models for more complex shapes. Droplets of three different crude oils, two medium oils, and one heavy oil were quantified and all droplets were oblate spheroids. The impact of the deviation from sphericity on the accuracy of each model was determined. If an inversion of the model for spherical droplets was used to estimate flux from acoustic observations, errors in the predicted volume of a droplet were between 30% and 50%. The heavy oil also showed deviations in predicted volume of 20%–40% when using the two models for more complex shapes. https://doi.org/10.1121/1.5121699

[JAC] Pages: 1176–1188

I. INTRODUCTION

Improved acoustic methodologies for the detection and quantification of oil in the marine environment are necessary for determining the extent and fate of oil spills, as well as the natural background level of oil in the marine environment. During the Deep Water Horizon (DWH) spill, high frequency (above 1 MHz) acoustic systems were deployed to the leaking well site to determine the flux of oil and gas from the wellhead (Camilli *et al.*, 2012). Lower frequency (200 kHz) ship mounted echosounders were also used to detect oil from a greater range and determine flux in the water column (Weber *et al.*, 2012). Both methods estimated a similar concentration of oil; however, they also relied on assumptions about the size and shape of droplets to determine flux from acoustic scattering. The present study aims to test these assumptions by comparing measured and modeled broadband acoustic backscatter from individual crude oil droplets with different, and known, sizes, shapes, and material properties.

Droplet size is crucial to determining fate and transport of oil in the marine environment, as it is a key component in determining both droplet rise rate and bioremediation rate. As droplet size decreases surface area to volume ratio increases exposing more oil to hydrocarbon consuming bacteria. In fact, oil spill responders take advantage of the enhanced bioremediation provided by smaller droplets by adding chemical dispersants to decrease droplet size. Estimates of the initial diameter of droplets released from the Deep Water Horizon (DWH) spill range from 300 μm to 10 mm for droplets formed without the addition of chemical dispersants, and from 10 to 1000 μm for droplets formed after the addition of dispersants (North *et al.*, 2015; Socolofsky *et al.*, 2011; Zhao *et al.*, 2014). The wide range of droplet size estimates is due in part to a lack of *in situ* verification of droplet size. Broadband acoustic backscatter measurements offer the opportunity to quantify oil droplet size *in situ*, which in turn will improve determination of the fate of oil in the marine environment.

Broadband acoustic backscatter has been used to differentiate between plankton and turbulent microstructure (Lavery *et al.*, 2010), quantify bubbles under breaking waves (Medwin and Breitz, 1989; Terrill and Melville, 2000; Vagle and Farmer, 1992), and as an aid for classifying fish species (Holliday, 1972; Stanton *et al.*, 2010; Thompson and Love, 1996). The quantification and classification of these targets relies on well constrained models of frequency dependent target strength (TS), a measure of the strength of backscatter that is a function of the target's size, shape, and contrast in sound speed and density between the target and the surrounding medium. TS is the ratio of the backscattered intensity to the incident intensity at 1 m from the target and is

a)Electronic mail: sloranger@ccom.unh.edu

independent of the incident power. The broadband TS of weak scatterers, such as oil droplets, has a characteristic peak and null structure where the amplitude of peaks and frequency of nulls are used to classify targets. Modeling the amplitude of peaks and frequency of nulls requires precise knowledge of the sound speed and density of oil, which at oceanographic conditions can be difficult to determine due to phase changes in oil. The sound speed and density are predictable for some oils at oceanographically relevant temperatures and pressures (Loranger *et al.*, 2018). If the impedance and shape are known, inversions of scattering models for individual scatterers can be used to determine the remaining model input: size.

Jech *et al.* (2015) and Stanton and Chu (2000) review a variety of acoustic scattering models of increasing complexity, both computationally and in terms of the target shape. Weber *et al.* (2012) used a simplified model of acoustic scattering that assumes droplets were spherical to determine oil flux during the DWH spill. However, oil droplets can vary in shape depending on the size and physical properties of the oil (Clift *et al.*, 1978; Pedersen, 2016). The degree to which oil droplets deviate from the spherical shape assumed by Weber *et al.* (2012) and the impact of the deviations on acoustic scattering and ultimate predictions of droplet size is unknown.

In this study broadband (100.5–442 kHz) acoustic backscatter from crude oil droplets in freshwater was measured. Droplets of varying material properties, size, and shape were generated by a novel droplet making device, and the size and shape were measured by a calibrated machine visions camera. The material properties of the oils were measured and described in Loranger *et al.* (2018). The measured TS of droplets was compared to three increasingly complex models of scattering from fluid targets: Anderson (1950) for simple spheres, the Distorted Wave Born Approximation (DWBA; Stanton *et al.*, 1998), an estimation of scattering for more complex shapes, and finally the boundary element method (BEM; Francis and Foote, 2003; Okumura *et al.*, 2003), a more computationally complex model for complex shapes, to determine how well each model agrees with empirically measured broadband backscatter.

II. MATERIALS

Three different crude oils, identified by geographic origin of the sample, were used in this study: Alaska North Slope (ANS), Angolan Xikomba (XIK), and Angolan Bavuca (BAV). Table I lists the properties of these oils at the experimental temperature, 21.6 °C, and atmospheric pressure based on measurements by Loranger *et al.* (2018). Viscosity was measured by a rotational viscometer (Brookfield Ametek LVDV1M Viscometer, Middleboro, MA; ASTM D7867-13, 2013). Surface tension for each oil in deionized water and simulated seawater (salinity 35 ppt; Kester *et al.*, 1967) was measured by the Center for Complex Fluids at Carnegie Mellon University (Alvarez *et al.*, 2010) at 21.0 ± 0.5 °C. The acoustic experiments were conducted in a 12 m × 18 m × 6 m (length × width × depth) freshwater tank at the University of New Hampshire (UNH). Properties of the tank water are listed in Table I. Temperature was measured by an RBRsolo T Temperature Logger (accuracy ± 0.002 °C; Ottawa, Ontario) and the sound speed was calculated according to Bilaniuk and Wong (1993). A nominal value of 998 kg/m^3 was assumed for density.

TABLE I. Physical properties of the fluids used in this study. All values are for atmospheric pressure and 21.6 °C. Interfacial tension values are for oil and simulated sea water/deionized water.

	ANS	XIK	BAV	Tank water
API gravity (°)	28.2	24.2	17.7	—
Density (kg/m^3)	878.5	875.7	942.2	998
Sound speed (m/s)	1399.7	1403.5	1471.1	1487.2
Viscosity (cP)	17.1	31.3	650.0	0.9
Surface tension (mN/m)	20.3/26.2	24.0/23.5	27.1/26.7	—

III. MODELS

The experimental results are compared to broadband backscattering modeled by three commonly used models: the modal solution derived by Anderson (1950), the DWBA (Stanton *et al.*, 1998), and the BEM (Francis and Foote, 2003; Okumura *et al.*, 2003). These three models have been used to predict the scattering from a variety of targets, for example, the Anderson (1950) model has been used to predict scattering from euphausiids and oil droplets (Kristensen and Dalen, 1986; Weber *et al.*, 2012), the DWBA has been used to predict the scattering from a variety of biological targets, including copepods, euphausiids, krill, and squid (Chu *et al.*, 1993; Jones *et al.*, 2009; Stanton and Chu, 2000), and the BEM has been used to model backscatter from bubbles, fish swimbladders, and swimbladder like shapes (see, e.g., Francis and Foote, 2003; Okumura *et al.*, 2003). The Anderson model assumes that targets have spherical symmetry, while the DWBA can be used for more complex shapes; however, it assumes that targets are weakly scattering. The BEM is valid for complex shapes and a variety of boundary conditions; however, it is much more computationally expensive than the Anderson (1950) model and the DWBA. For all of the models it is assumed that the material properties are homogeneous throughout the droplet, and the effects of dispersion and attenuation within the target are negligible.

The droplets in this experiment rose to the surface with their axis of symmetry perpendicular to the water surface and the incident and reflected waves traveled parallel to the axis of symmetry. Experimental results were limited to droplets that were within three degrees of the maximum response angle of the transducer, and therefore the maximum deviation from normal incidence is three degrees, a deviation that does not significantly impact model results (Fig. 1). The DWBA and BEM were computed for droplets that are oblate spheroids and the Anderson model for equivalent volume spheres.

The subscripts t and w below indicate that the variable is in reference to the target or surrounding medium, respectively. The details of the models below are intended to

provide a physical insight into the model methodologies and are in no way meant to be a rigorous derivation.

A. Anderson sphere model

Taking advantage of the symmetry of a spherical target, Anderson (1950) calculated the exact modal solution for sound scattering from a plane wave incident on a fluid sphere. The exact solution for the backscattering form function, f_{bs}, in the far field from a fluid filled sphere is

$$f_{bs} = -\frac{i}{k_w}\sum_{n=0}^{\infty}(-1)^n(2n+1)A_n, \tag{1}$$

where k_w is the acoustic wavenumber of the surrounding medium and

$$A_n = \frac{-1}{1+iC_n}, \tag{2}$$

where

$$C_n = \frac{\left[j_n'(k_t a)y_n(k_w a)\right]/\left[j_n(k_t a)j_n'(k_w a)\right] - gh\left[y_n'(k_w a)/j_n'(k_w a)\right]}{\left[j_n'(k_t a)j_n(k_w a)\right]/\left[j_n(k_t a)j_n'(k_w a)\right] - gh}. \tag{3}$$

j_n is the spherical Bessel function of the first kind of order n where a prime denotes the derivative with respect to the argument, and y_n is the spherical Neumann function where a prime denotes the derivative with respect to the argument. k is the acoustic wavenumber of the target, a is the radius of the sphere, g is the density ratio (ρ_t/ρ_w), h is the sound speed ratio (c_t/c_w), ρ is the density, and c is the sound speed. The subscripts t and w denote the target and surrounding medium, respectively.

The TS is related to f_{bs} by

$$\mathrm{TS} = 10\log_{10}\left(|f_{bs}|^2\right). \tag{4}$$

The Anderson model in this study was evaluated by taking the sum of the first $ka + 20$ terms ($n = ka + 20$), which provides for convergence of the solution relative to a precision of 0.1 dB (Jech *et al.*, 2015).

B. DWBA

Scattering from a plane wave incident on the target can be approximated by the DWBA. The Born approximation assumes that a target is weakly scattering and therefore the total field at a point is approximately equal to the incident field. For the DWBA, scattering is calculated with the magnitude of the incident acoustic wavenumber determined by the sound speed of the scatterer (hence, the term distorted). The DWBA is valid over all ranges of angles of incidence (Stanton and Chu, 2000; Stanton *et al.*, 1998) when differences between the properties of the target and the surrounding medium are small. The general form of the Born approximation is a volume integral derived by Morse and Ingard (1968),

$$f_{bs} = \frac{k_w^2}{4\pi}\int_v\int\int(\gamma_\kappa - \gamma_\rho)e^{2i(\vec{k}_i)\cdot\vec{r}_v}\,dv, \tag{5}$$

where γ_κ is the compressibility parameter $[(\kappa_t - \kappa_w)/\kappa_w]$ and κ is compressibility $[(\rho c^2)^{-1}]$, γ_ρ is the density parameter $[(\rho_t - \rho_w)/\rho_t]$, $(\vec{k}_i)$ is the incident acoustic wavenumber vector, $\vec{r}_v$ is the position vector of the volume, and v is the volume of body. The DWBA replaces $(\vec{k}_i)$ with the wavenumber vector whose magnitude is determined by the material properties of the target $(\vec{k}_i)_t$ (Stanton *et al.*, 1993). Stanton *et al.* (1998) solve the volume integral for an object whose cross section is circular at every point along the lengthwise axis (i.e., a cylinder or disk) where the radius of the cross section can vary as a function of position on the lengthwise axis (a deformed cylinder or disk; Fig. 2). For an unbent cylinder, such as an oblate spheroidal oil droplet, the volume integral reduces to a line integral

$$f_{bs} = \frac{k_w}{4}\int_{\vec{r}_{pos}}(\gamma_\kappa - \gamma_\rho)e^{2i(\vec{k}_i)_t\cdot\vec{r}_{pos}} \times a\frac{J_1(2k_t a\cos\theta)}{\cos\theta}|d\vec{r}_{pos}|, \tag{6}$$

where $\vec{r}_{pos}$ is the position vector of the axis of the cylinder, J_1 is the spherical Bessel function of the first kind of order 1, and θ is the angle of orientation of the body relative to the direction of the incident wave. The droplets in this study had an unbent axis of symmetry parallel to the direction of travel of the incident and reflected waves resulting in end-on ensonification for all cross sections. For end-on ensonification, where the incident wave is in the same direction as r_{pos}, θ is

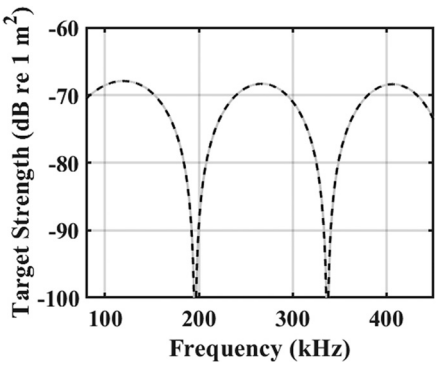

FIG. 1. The impact of a change in an incident angle of three degrees. The solid gray line is modeled results using the DWBA for a plane wave incident on an ANS oil droplet with normal incidence. The dashed black line is for the same oil droplet with a plane with incident at three degrees from normal.

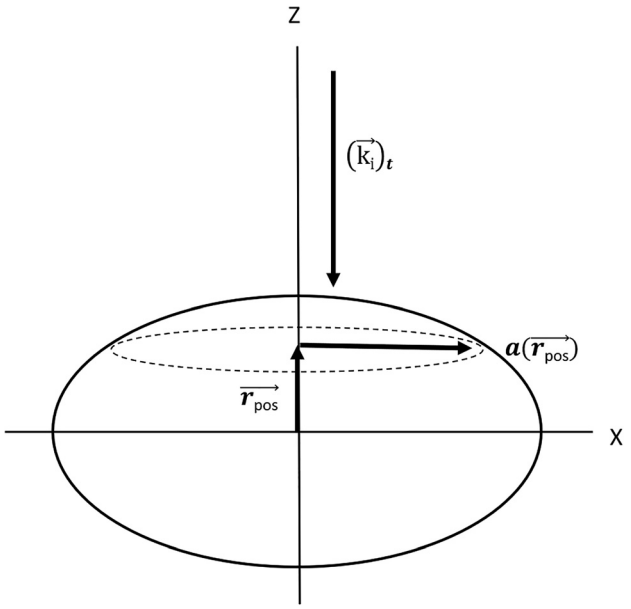

FIG. 2. Geometry of incident wave, $(\vec{k}_i)_t$, and an oblate oil droplet for end-on ensonification for use in the DWBA. $r_{pos}^{\rightarrow}$ is the position vector and $a(r_{pos}^{\rightarrow})$ is the radius of cylinder of thickness $dr_{pos}^{\rightarrow}$, at position $r_{pos}^{\rightarrow}$.

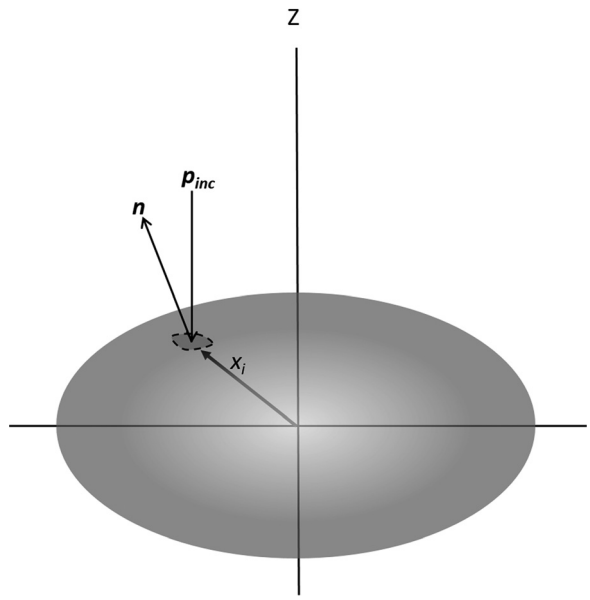

FIG. 3. Geometry of incident wave, p_{inc}, on a droplet in domain Ω with surface Γ. Γ is divided into surface elements such as the element at location $\mathbf{x_i}$ seen here with a vector normal to the element surface n. The incident wave travels parallel to the axis of symmetry of the oblate spheroidal droplet. The backscattered wave also travels parallel to the axis of symmetry but in the opposite direction.

equal to 90° (0° is broadside incidence), and the dot product $(\vec{k}_i)_t \cdot \vec{r}_{pos}$ reduces to $|k_t||r_{pos}|$. The discontinuity in the integral at 90° can be approximated by calculating the limit of f_{bs} as it approaches 90° from both sides. The integral solution was approximated with a rectangle rule, using cross sections of thickness 1 μm, less than 1/1000 of a wavelength for all frequencies.

C. BEM

The BEM breaks the surface of a target into a finite number of geometric shaped elements (Fig. 3). It can be used to approximate scattering of an incident plane wave from arbitrary shapes.

For computing the BEM, three-dimensional (3-D) simulations of droplets were generated using MATLAB and the surface of the simulation was meshed using Netgen v5.3. The number of mesh nodes per acoustic wavelength exceeded ten for the shortest wavelengths used during simulation. Convergence tests were performed with varying mesh densities performed prior to the simulations. The acoustic wave equation was solved using a computational boundary element platform (BEM++ v 2.0.3; Śmigaj *et al.*, 2015) for a plane wave incident on the droplet and traveling parallel to the radius of symmetry of the droplet.

A droplet in domain Ω with surface Γ and sound speed c_t and density ρ_t was embedded in an infinite homogenous isotropic medium with sound speed c_w and density ρ_w. Propagation of time harmonic acoustic waves is described by the Helmholtz equation for the interior and exterior of the droplet as

$$\Delta p(\mathbf{x}) + k_{\text{int}}^2 p(\mathbf{x}) = 0, \quad \forall \mathbf{x} \in \Omega, \tag{7}$$

$$\Delta p(\mathbf{x}) + k_{\text{ext}}^2 p(\mathbf{x}) = 0, \quad \forall \mathbf{x} \in R^3 \backslash \Omega, \tag{8}$$

where k_t and k_w are the acoustic wavenumber of the droplet and embedding medium, respectively, and $p(\mathbf{x})$ is the pressure perturbation of the element on the droplet surface at $\mathbf{x}$. Boundary conditions on the surface Γ are given by

$$\gamma_0^{\text{int}} p(\mathbf{x}) = \gamma_0^{\text{ext}} p(\mathbf{x}), \quad \forall \mathbf{x} \in \Gamma, \tag{9}$$

$$\rho_{\text{int}}^{-1} \gamma_1^{\text{int}} p(\mathbf{x}) = \rho_{\text{ext}}^{-1} \gamma_1^{\text{ext}} p(\mathbf{x}), \quad \forall \mathbf{x} \in \Gamma, \tag{10}$$

where γ_0 and γ_1 are the Dirchlet and Neumann traces, respectively, and the superscripts "int" and "ext" refer to the interior and exterior of the target, respectively.

The backscattered pressure $p_{\text{scat}}(\mathbf{x})$, generated by an incident plane wave described by $p_{\text{inc}}(\mathbf{x})$ incident on the droplet, fulfills the Helmholtz equation for the embedding domain

$$p(\mathbf{x}) = p_{\text{scat}}(\mathbf{x}) + p_{\text{inc}}(\mathbf{x}), \quad \forall \mathbf{x} \in R^3 \backslash \Omega, \tag{11}$$

with the scattered pressure field fulfilling Sommerfeld's radiation condition at infinity,

$$\lim_{|x| \to \infty} = \left[\frac{\partial}{\partial |x|} p_{\text{scat}}(x) - i k_{\text{ext}} p_{\text{scat}}(x) \right] = 0. \tag{12}$$

The integral-equation formulations utilized for the simulations of backscatter from the oil droplets are described by Eq. (30) in Śmigaj *et al.* (2015), which is taken from Kleinman and Martin [1988, Eq. (4.9)] and first proved solvable by Costabel and Stephen (1985), and is free from the irregular frequency problem. This implementation was validated for weakly scattering targets against the prolate spheroid modal series (PSMS) model computed from 12 to 200 kHz (Jech *et al.*, 2015). BEM++ uses adaptive cross approximation to speed up the solution of the Helmholtz equation.

IV. EXPERIMENTAL METHODS

A. Droplet generation

A droplet making device was designed and built for the generation of individual oil droplets of a consistent and adjustable size (Fig. 4). The droplet maker consisted of an oil reservoir and needle manifold. A compressed air source was connected to the reservoir via a precision air pressure regulator, which supplied sufficiently high pressure to push the viscous oil through the reservoir and needle manifold while being kept low enough to release only individual droplets. Minor adjustments to air pressure allowed for control of the release rate of droplets, limiting the rate so that only a single droplet was present in the water column at any given time.

Droplet size was controlled by the size of needles through which oil was released. The interior radius of the needle, pressure applied by the air source, and surface tension of the oil determined the droplet size. Larger needle size resulted in larger droplets for an individual oil, while an oil with higher surface tension resulted in larger droplets emanating from the same needle size compared to a lower surface tension oil. A circular manifold of four different sized needles was connected to the oil reservoir. A drive belt connected the needle manifold to a stepper-motor that was controlled from the surface, allowing the user to change the needle size without recovering the droplet making system from the bottom of the tank. Once aligned, oil could only pass through the selected needle.

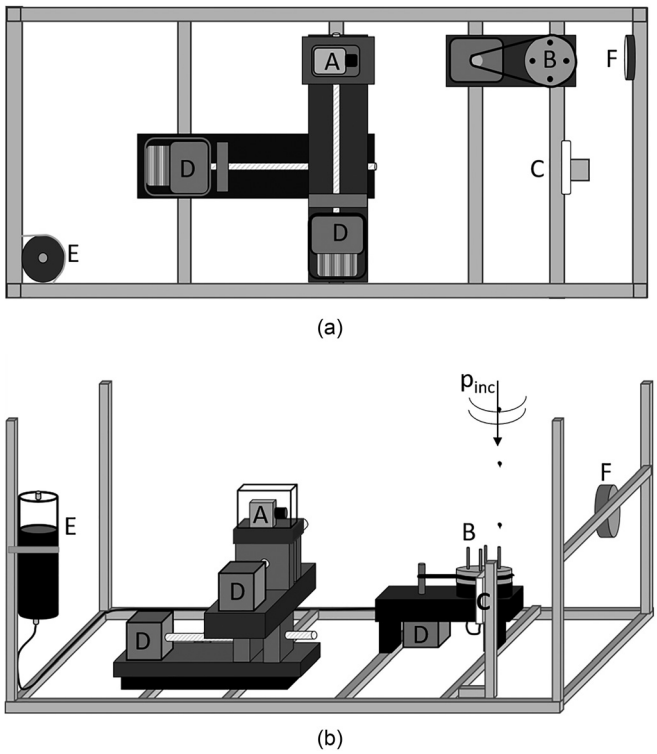

FIG. 4. (a) Top down view and (b) side on perspective of droplet making and imaging system. (A) High definition machine vision camera. (B) Needle rosette. (C) Calibration target. (D) Stepper motors. (E) Oil Reservoir. (F) LED light panel. The stepper motors on the camera platform move the camera in two dimensions parallel to the bottom of the platform. The camera is moved perpendicular to the face of the calibration target to focus on the plane containing the target and needle. The camera is then moved from the calibration target to the needle rosette. p_{inc} indicates the direction of the incident wave from the echo sounders at the tank surface.

The filled reservoir and needle rosette, along with the imaging system described in Sec. IV B were deployed to the bottom of the 12 m × 18 m × 6 m (length × width × depth) fresh water tank at UNH and allowed at least an hour to equilibrate with the tank. Tank temperature was measured by two RBR (Ottawa, Ontario) temperature probes, one at the surface and one attached to the droplet making system. Once released, droplets rose to the surface of the tank where they were collected for disposal.

B. Imaging system

As the droplets were released from the needle manifold the size was measured by a calibrated machine vision camera (Edmond Optics EO-1312 1.3 Megapixel Color USB 3.0 camera with C Series 25 mm fixed focal length imaging lens, Barrington, NJ; Fig. 4). The machine vision camera had a very narrow depth of field (1.5 cm between the front and back focal planes) so that objects in focus in the foreground were of similar size to objects in focus in the background. The camera sat atop a platform that allowed the camera to be moved in two dimensions parallel to the tank bottom. Two stepper motors controlled from the surface of the tank were used to position the camera. One motor was used to focus the fixed focal length camera by moving the camera toward and away from a target, and the other motor was used to move the camera in the perpendicular direction to position the target in the center of the frame.

The camera system was calibrated by focusing on a 3-D printed checkerboard of two-millimeter boxes that filled the camera frame, positioned at the same range from the camera face as the oil-releasing needle. The camera position was adjusted so that the calibration target was in the center of the focal plane. The camera recorded a still-frame image of the checkerboard at the bottom of the tank, and the vertical and horizontal pixel size of the image was calibrated and analyzed to check for image distortion. The mean pixel size for both vertical and horizontal pixels was found to be 0.0476 ± 0.0006 mm/pixel and no measurable distortion in the rectified images was detected. The error in the pixel size measurement (±0.0006 mm/pixel) was equal to the difference in pixel size between the foreground and background focal planes (0.0012 mm/pixel).

A light-emitting diode (LED) light panel backlit the droplets to maximize the contrast between droplets and the background. Individual frames from the recorded video were analyzed in MATLAB. Each frame containing a droplet was converted to gray scale, normalized to the maximum intensity in the frame and then converted to a binary image with threshold of 0.17. Droplets were defined by finding components with a connectivity of eight pixels. The boundary, centroid, major radius, minor radius, and orientation of the radii were then estimated for each droplet (Fig. 5). Images containing droplets were manually scrutinized to remove erroneous detections (e.g., where the droplet was too far to the side of the frame to be adequately characterized, another object was in frame, or some other anomalous issue resulted in an inadequate characterization of a droplet).

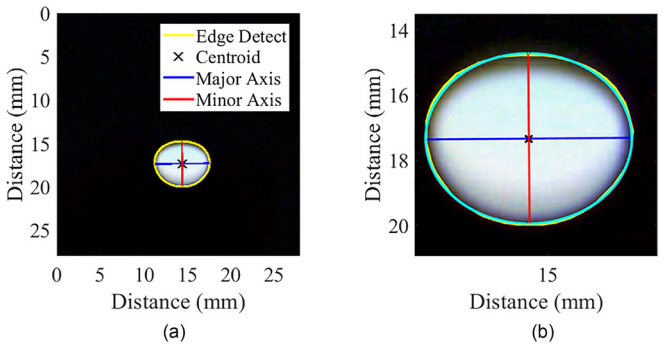

FIG. 5. (Color online) (a) Image processing example for oil droplet. Droplets are released at a rate so that only a single droplet is in frame. (b) Zoom in on the droplet from (a) with the outline of the assumed oblate spheroid shape overlaid (medium gray outline, cyan online) showing how well the oblate shape fits the edge detect (light gray outline, yellow online).

The calibration of the imaging system was verified using opaque black spherical beads. Individual beads were manually dropped through a syringe and fell through water in the focal plane of the camera. Three or four frames were captured for each bead. The major and minor radii for each frame containing a bead were calculated using the above method, and the three or four measurements of each bead averaged together. The major and minor radii calculated by the imaging system were then compared to measurements made by a Mitutoyo PH-A14 Horizontal Profile Projector (Kanagawa, Japan) in air. Two different bead size ranges were used. The major radius of the larger calibration spheres varied from 1.024 to 1.247 mm (0.910 to 1.081 mm minor radius) and the smaller spheres had a major radius range of 0.616 to 0.694 mm (0.539 to 0.673 mm minor radius) according to the projector. For all targets, the root-mean-square (RMS) error between the camera and microscope measurements of the major and minor radii was 0.028 mm (a little over half a pixel), and there was no relationship between error and target size.

C. Broadband acoustic system

Three Kongsberg (Kongsberg, Norway) split-beam, piston-type transducers, an ES120, ES200, and ES333, were mounted at the surface of the UNH freshwater tank inside of an oil collection ring. Each of the three transducers has a 7° (one-way) beam pattern at its center frequency (120 kHz, 200 kHz, and 333 kHz). The transducers were connected to Kongsberg EK80 wide band transceivers (WBTs), enabling broadband transmission and reception on the three echo sounders. One millisecond linear frequency modulated (LFM) pulses were sequentially transmitted from each transducer with bandwidths covering 95–150 kHz, 160–250 kHz, and 280–450 kHz. The WBTs apply a Tukey window to the transmit signal, resulting in tapered regions within the transmitted frequencies. The low signal-to-noise ratio (SNR) in the tapered region resulted in the exclusion of those frequencies from analysis. The ratio of the tapered bandwidth to total transmitted bandwidth was 0.20, 0.13, and 0.11 for the ES120, ES200, and ES333, respectively. Data analysis was restricted to frequencies not in the tapered region: 100.5–145.5, 166.5–244.5, and 290–442 kHz for the ES120, ES200, and ES333, respectively. The transducers were calibrated using standard size spheres according to the method described by Demer *et al.* (2015). Transducers were positioned directly above the droplet making system so that droplets were ensonified from above as they rose to the tank surface.

The waveforms from the four quadrants recorded by the WBTs were summed and match filtered using an idealized transmit signal (Weber and Ward, 2015). Droplets were identified in the echogram and the Fourier transform computed for 250 samples around each droplet, avoiding the transmit pulse and bottom return. The resulting frequency resolution for the ES120 and ES200 was 500 Hz and 1 kHz for the ES333. The frequency domain results were range corrected for spherical spreading and frequency dependent absorption (Francois and Garrison, 1982).

V. RESULTS

A. Droplet size

An average of 4.5 video frames were recorded for each droplet. The major and minor radii were measured for each frame and averaged together for each droplet in the same manner as the bead calibration. The radius of a sphere of equivalent volume was calculated for each frame from the major and minor radii and averaged together in the same manner.

Individual droplet sizes were not evenly distributed between the maximum and minimum droplet sizes for a given oil. There were four main divisions of droplets, one for each of the four needles. Within each of the main divisions, droplets were sorted into 100 μm (approximately 2 pixel) wide groups by the droplet's major radius (Fig. 6). The droplets were grouped to save computing time for BEM. The occurrence of multiple groups of droplets for a single needle was the result of changes to the pressure applied to the droplet making system to change droplet release rate during droplet formation. The mean and standard deviation of the major radius, minor radius, and radius of a sphere of equivalent volume for the droplets within each group were calculated (Tables II–IV). The 95% confidence interval was calculated assuming that all grouped droplets were normally distributed about the group mean. BAV, which had the highest viscosity and surface tension, resulted in the largest droplets for a given needle size, while ANS and XIK resulted in similar distributions of droplets that were smaller than BAV. The eccentricity, ε,

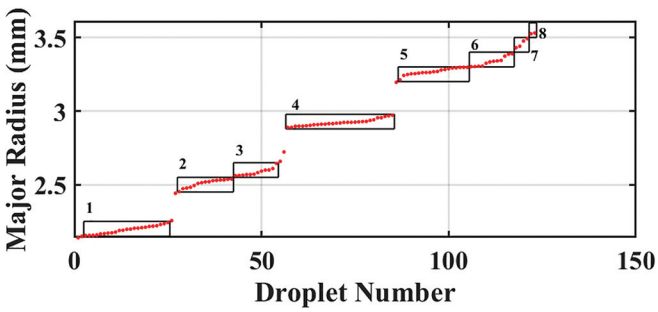

FIG. 6. Grouped major radius results for XIK. Sorted major radii for all droplets (red circles) organized into 100 μm wide groups (black boxes) with group number labeled, showing the uneven distribution of radii across the size range and within groups.

TABLE II. Droplet size and shape for ANS according to the machine vision camera system. Equivalent radius is for a sphere of equivalent volume. N is the number of observations in the 100 μm group. All radii and confidence intervals are in mm. All confidence intervals are calculated for $\alpha = 0.05$. Rise velocity (U) is in m/s.

a_{maj}	a_{min}	r_{eq}	ϵ	N	Re/Eo/log(M)	U
2.39 ± 0.07	2.08 ± 0.04	2.28 ± 0.06	0.49	6	480/0.9/−10.3	0.100 ± 0.005
2.47 ± 0.05	2.14 ± 0.06	2.35 ± 0.05	0.50	9	470/1.0/−10.3	0.096 ± 0.004
2.59 ± 0.04	2.24 ± 0.07	2.47 ± 0.05	0.50	6	500/1.1/−10.3	0.097 ± 0.004
2.74 ± 0.05	2.31 ± 0.06	2.59 ± 0.04	0.54	26	570/1.2/−10.3	0.105 ± 0.009
2.85 ± 0.06	2.37 ± 0.09	2.68 ± 0.07	0.56	15	610/1.3/−10.3	0.108 ± 0.007
2.95 ± 0.06	2.44 ± 0.03	2.77 ± 0.04	0.56	6	620/1.4/−10.3	0.108 ± 0.007
3.14 ± 0.06	2.55 ± 0.09	2.93 ± 0.04	0.58	8	700/1.5/−10.3	0.114 ± 0.007
3.23 ± 0.04	2.56 ± 0.12	2.99 ± 0.06	0.61	8	710/1.6/−10.3	0.114 ± 0.009
3.50 ± 0.01	2.87 ± 0.04	3.27 ± 0.02	0.57	5	720/1.9/−10.3	0.105 ± 0.002

$$\epsilon = \sqrt{1 - \frac{a_{min}^2}{a_{maj}^2}}, \tag{13}$$

where a_{min} is the minor radius and a_{maj} is the major radius, was then calculated for each binned droplet. The oil droplets were approximately oblate spheroids with eccentricities between 0.42 and 0.63. BAV was the least eccentric oil with no values above 0.5, and eccentricity increased with droplet size for all oils.

The droplet measurements were compared to the droplet shape and size predicted by Clift *et al.* (1978), who used three non-dimensional numbers to describe the shape of particles: the Reynolds (Re), Eötvös (Eo) or Bond, and Morton (M) numbers. Each number is a function of the physical properties of the particle and the surrounding medium:

$$\mathrm{Re} = \frac{\rho_w d_e U}{\mu_w}, \quad \mathrm{Eo} = \frac{G\Delta\rho_w d_e^2}{\sigma}, \quad M = \frac{g\mu_w^4 \Delta\rho}{\rho_w^2 \sigma^3}, \tag{14}$$

where d_e is the diameter of the particle (major diameter for rising oblate spheres), U is the rise rate, μ_w is the dynamic viscosity of the surrounding medium, g is gravitation acceleration, $\Delta\rho$ is the difference in density between the particle and surrounding medium, and σ is the interfacial tension of particle in the surrounding medium. The rise rate was calculated from the transducer observations by dividing the distance a droplet rises between pings by the time between pings. The three non-dimensional numbers converge as predicted by Clift *et al.* (1978) in the region between spheres and wobbling ellipsoidal particles. This agrees well with the oblate spheroid shape measured by the camera.

B. Frequency response

The two features of the broadband frequency response used to quantify targets are the amplitude of peaks and frequency of nulls. These two features were identified in the measured backscatter as well as in the three models. The amplitude of the peak and frequency of nulls in the measurements were then compared to the modeled peaks and nulls to determine whether or not those features differed significantly between the model and measured backscatter. Differences between the measured and modeled results indicate that inversions of the models would result in errors in predicting the droplet size based on the broadband backscatter.

The intensity at each frequency for all pings of an individual droplet was averaged together. Figure 7 shows the TS calculated for each of 20 pings incident on a 2.93 mm equivalent radius ANS droplet as well as the average intensity of those 20 pings in dB. 83% of the backscatter measurements at a given frequency were within 30% of the mean intensity (corresponding to the mean TS +1.1 dB/−1.5 dB). As TS decreased (near nulls), the width of the distribution of TS measurements about the mean increased. When the mean TS value at a given frequency was below −85 dB, 74% of measurements were within 30% of the mean intensity.

The imaging system and broadband acoustic system were time synced so that the droplet size and shape from the imaging system for a single droplet corresponded with the TS measurement from the broadband acoustic system. The TS measurements were sorted with the droplet size and shape data into groups by the major radius as described above. The intensity was then averaged for all droplets in a

TABLE III. Droplet size and shape for XIK according to the machine vision camera system. Equivalent radius is for a sphere of equivalent volume. N is the number of observations in the 100 μm group. All radii and confidence intervals are in mm. All confidence intervals are calculated for $\alpha = 0.05$. Rise velocity (U) is in m/s.

a_{maj}	a_{min}	r_{eq}	ϵ	N	Re/Eo/log(M)	U
2.19 ± 0.05	1.90 ± 0.07	2.09 ± 0.06	0.50	23	380/0.9/−10.1	0.087 ± 0.006
2.51 ± 0.05	2.08 ± 0.07	2.36 ± 0.05	0.56	15	450/1.1/−10.1	0.091 ± 0.004
2.59 ± 0.05	2.13 ± 0.07	2.42 ± 0.05	0.57	12	470/1.2/−10.1	0.093 ± 0.004
2.92 ± 0.05	2.39 ± 0.12	2.73 ± 0.06	0.58	29	540/1.5/−10.1	0.095 ± 0.005
3.27 ± 0.05	2.58 ± 0.13	3.02 ± 0.06	0.61	19	660/1.9/−10.1	0.105 ± 0.006
3.34 ± 0.06	2.59 ± 0.11	3.07 ± 0.07	0.63	12	690/1.9/−10.1	0.108 ± 0.006
3.46 ± 0.06	2.77 ± 0.23	3.21 ± 0.11	0.60	4	750/2.1/−10.1	0.112 ± 0.007
3.51 ± 0.05	2.81 ± 0.03	3.26 ± 0.04	0.60	2	750/2.2/−10.1	0.110 ± 0.006

TABLE IV. Droplet size and shape for BAV according to the machine vision camera system. Equivalent radius is for a sphere of equivalent volume. N is the number of observations in the 100 μm group. All radii and confidence intervals are in mm. All confidence intervals are calculated for $\alpha = 0.05$. Rise velocity (U) is in m/s.

a_{maj}	a_{min}	r_{eq}	ϵ	N	Re/Eo/log(M)	U
3.33 ± 0.04	3.01 ± 0.11	3.22 ± 0.06	0.42	20	520/0.9/−10.6	0.077 ± 0.006
3.39 ± 0.07	3.07 ± 0.07	3.28 ± 0.05	0.43	10	530/0.9/−10.6	0.077 ± 0.003
4.06 ± 0.05	3.68 ± 0.07	3.93 ± 0.04	0.43	3	710/1.3/−10.6	0.086 ± 0.002
4.15 ± 0.05	3.73 ± 0.15	4.01 ± 0.07	0.44	7	740/1.3/−10.6	0.089 ± 0.008
4.25 ± 0.06	3.84 ± 0.08	4.11 ± 0.06	0.43	9	800/1.4/−10.6	0.094 ± 0.004
4.35 ± 0.03	3.88 ± 0.20	4.18 ± 0.07	0.45	4	820/1.4/−10.6	0.094 ± 0.012
4.62 ± 0.04	4.23 ± 0.11	4.48 ± 0.06	0.40	8	850/1.7/−10.6	0.091 ± 0.004
4.70 ± 0.06	4.26 ± 0.11	4.55 ± 0.07	0.43	6	870/1.7/−10.6	0.091 ± 0.013
4.81 ± 0.09	4.34 ± 0.06	4.65 ± 0.05	0.43	6	890/1.8/−10.6	0.091 ± 0.006
4.91 ± 0.06	4.38 ± 0.15	4.72 ± 0.09	0.45	4	910/1.8/−10.6	0.093 ± 0.011
5.00 ± 0.02	4.39 ± 0.05	4.79 ± 0.03	0.48	4	930/1.9/−10.6	0.093 ± 0.010

group. Examples of acoustic results from a grouped droplet of each oil are shown in Fig. 8.

The DWBA and BEM model were then calculated for an oblate sphere with dimensions equal to the grouped major and minor radii, while the Anderson (1950) model was calculated for the grouped radius of a sphere of equivalent volume (Fig. 8). The peak of the modeled TS of each droplet was compared to the peak of the measured TS (Fig. 9). All models were computed for 80–450 kHz with 500 Hz spacing for the Anderson (1950) model and DWBA and 2 kHz spacing for the BEM. The BEM was computed at larger frequency spacing due to constraints on available computational time. The peak of the measured response was determined by the MATLAB mspeaks function, which uses wavelet denoising to smooth the signal, and then finds the center of mass of peaks using a user defined peak proportion (20% for this study) to determine the centroid of the peak (Coombes *et al.*, 2005; Morris *et al.*, 2005). Measured peaks within 10 kHz of the gap in frequencies between transducers were excluded because it was not possible to determine whether the peak was in the gap or not.

To determine the accuracy of each model when inverted for droplet size Figs. 10–12 compare the frequency of nulls from the modeled TS to the frequencies of nulls determined experimentally. An offset between the modeled and measured TS indicates that the inversion would results in an error in droplet size estimate. Null frequency was determined by inverting the TS plot and using the MATLAB mspeaks function as described above. Experimental data with nulls within 10 kHz of the gap in frequencies between transducers were excluded because it was not possible to reliably determine if the null was in the gap or not.

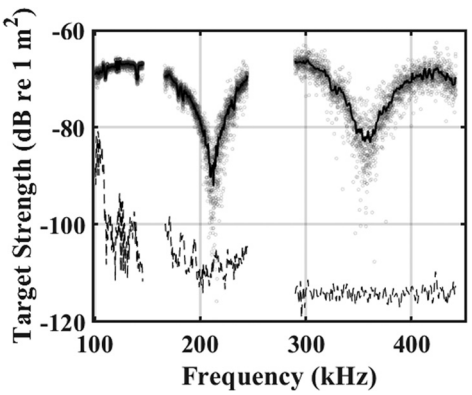

FIG. 7. Frequency response for a single ANS droplet of equivalent radius 2.93 mm. Transparent gray circles are from individual pings, and darker circles indicate higher data density. The black line is the mean intensity calculated at each frequency. The dotted lines indicate the noise floor of the three transducers.

To determine the variability of the predicted null frequency due to measurement error the three models were run for grouped droplet sizes measured by the imaging system at the 95% confidence limits (Tables II–IV). For the Anderson (1950) model, these limits represent two simple cases: droplet size was either underestimated or overestimated. These cases represent the frequency range over which the null would be expected to occur for a droplet with an equivalent radius within the 95% confidence limit of the measured droplet size (Figs. 10–12). For oblate shapes the confidence limits were evaluated for four different cases: (1) droplet size is underestimated by both the minor and major radius; (2) droplet size is overestimated by both the minor and major radii; (3) the droplet is more oblate than measured by underestimating the major radius and overestimated the minor radius; and (4) the droplet is more spherical than measured due to overestimating the major radius and underestimating the minor radius. These cases were evaluated at the 95% confidence limits for the mean major and minor radii as appropriate. According to the model results, cases (3) and (4) represent the more extreme limits of the confidence interval and are shown in Figs. 10–12.

VI. DISCUSSION

The BEM is a slightly better predictor of the amplitude of the peak of the TS response than the DWBA, and both the BEM and DWBA are slightly better predictors of peak TS than Anderson (1950). The RMS error between the modeled and predicted peak backscattering cross section for all peaks (excluding peaks within 10 kHz of the gap in frequencies between transducers) was 1.8 dB, 1.0 dB, and 0.5 dB for Anderson (1950), the DWBA, and the BEM, respectively. The Anderson (1950) model does not accurately predict the null frequency for the oblate oil spheres in this study. RMS

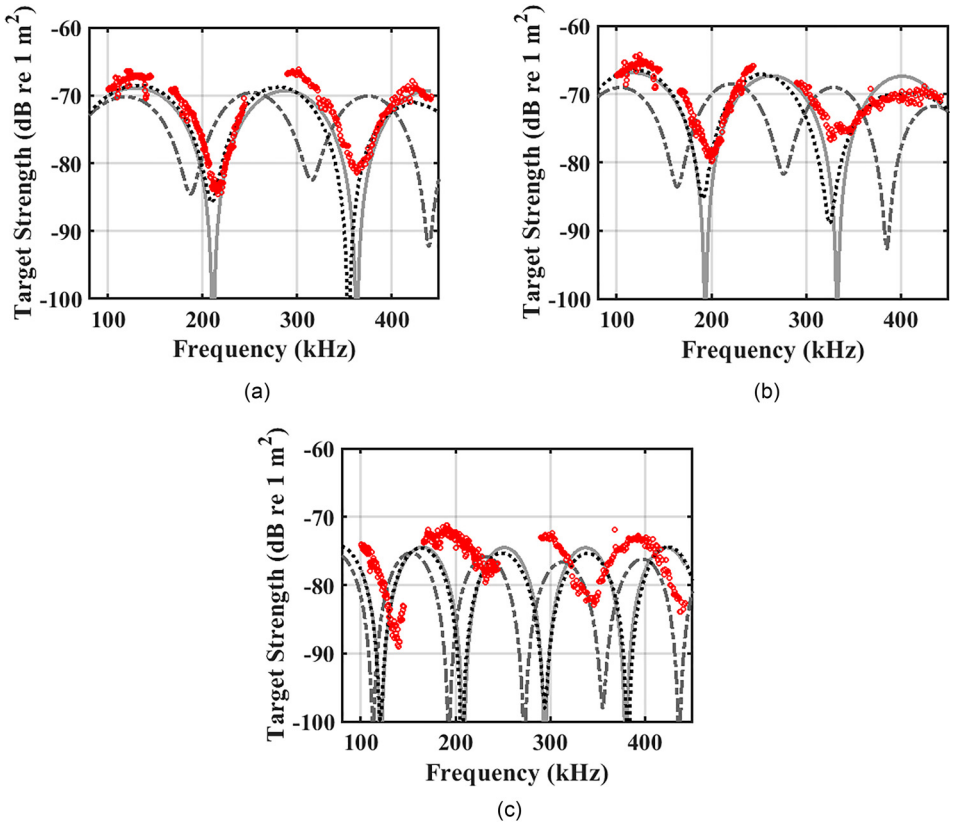

FIG. 8. (Color online) Recorded scattering (red circles) compared to Anderson (1950; dashed gray line), DWBA (solid gray line), and BEM (dotted black line). (a) ANS: equivalent radius: 2.68 mm. (b) XIK: equivalent radius: 3.07 mm. (c) BAV: equivalent radius: 4.65 mm.

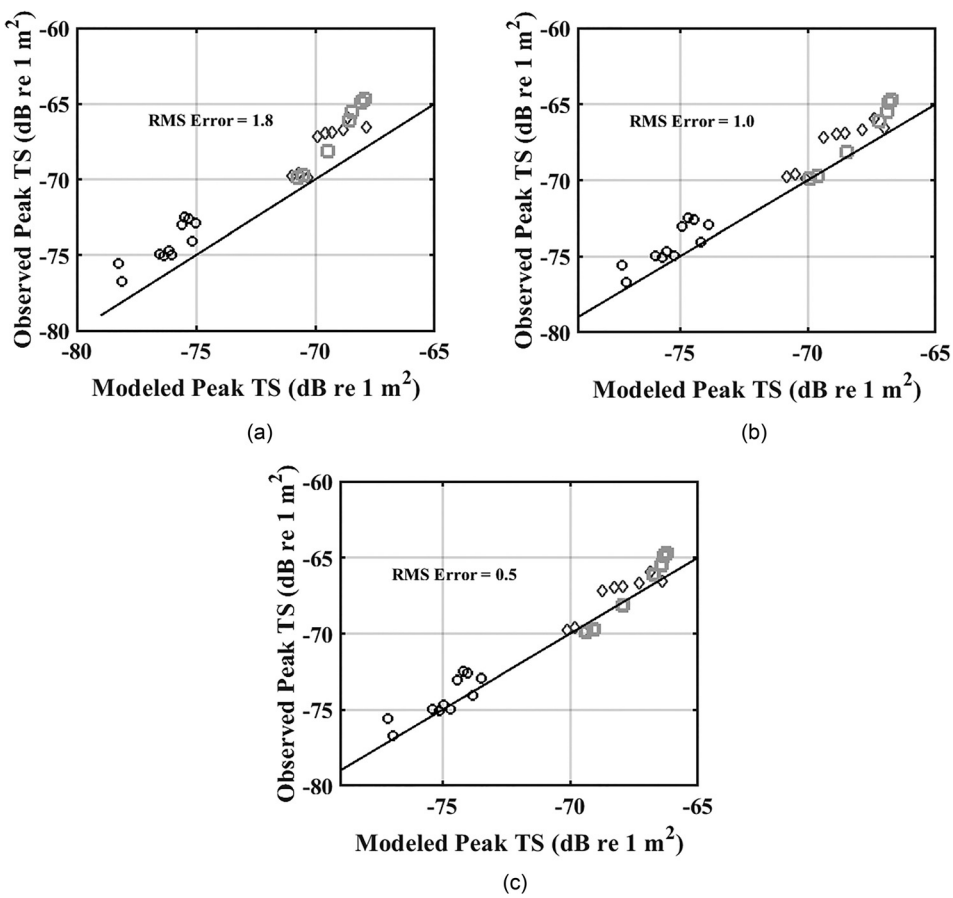

FIG. 9. Peak amplitude of the measured TS compared to the peak of (a) Anderson (1950), (b) the DWBA, and (c) the BEM. ANS (dark gray diamonds), XIK (light gray squares), and BAV (black circles) are compared to unity (black line). The RMS error between all measurements and the modeled peak is listed for each model.

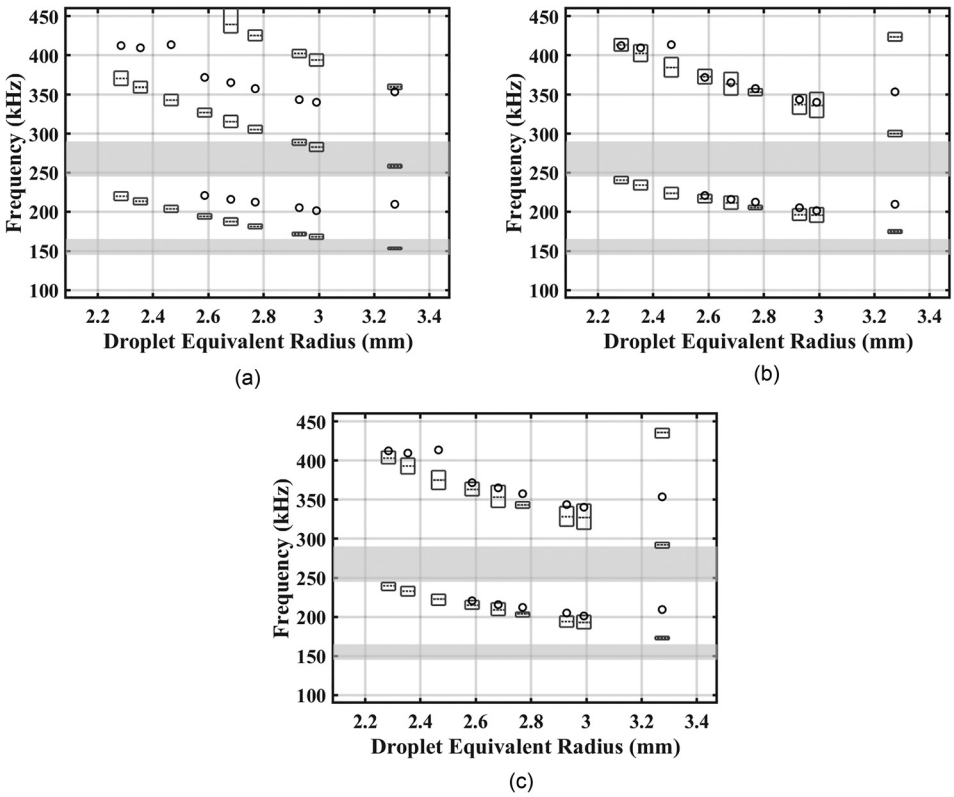

FIG. 10. The frequency of the null for all grouped ANS droplets compared to the modeled null frequency. The gray boxes show the range of the frequency off the null computed at the 95% confidence limits of the droplet size as measured by the imaging system. The dashed gray line in the gray box shows the null frequency for the mean droplet size. The null frequency from the measured backscatter is shows with a black circle. The modeled null frequencies are for (a) Anderson (1950), (b) DWBA, and (c) the BEM. The gray bands indicate the gap in ensonified frequencies between transducers. For recorded data, nulls detected within 10 kHz of the gap in frequencies between transducers are excluded.

error between the measured and modeled frequency of nulls for all measured nulls (excluding nulls within 10 kHz of the gap in frequencies) predicted by Anderson (1950) was 51 kHz, 53 kHz and 52 kHz, for ANS, XIK, and BAV, respectively. The DWBA and BEM provide better agreement between frequency of the predicted and observed null for ANS and XIK droplets, with RMS error between the measured null frequency and null frequency predicted by the BEM of 23 kHz and 17 kHz for ANS and XIK, respectively. For the DWBA, the RMS error between the measured null frequency and predicted null frequency was 19 kHz and 11 kHz for ANS and XIK, respectively. If the largest ANS

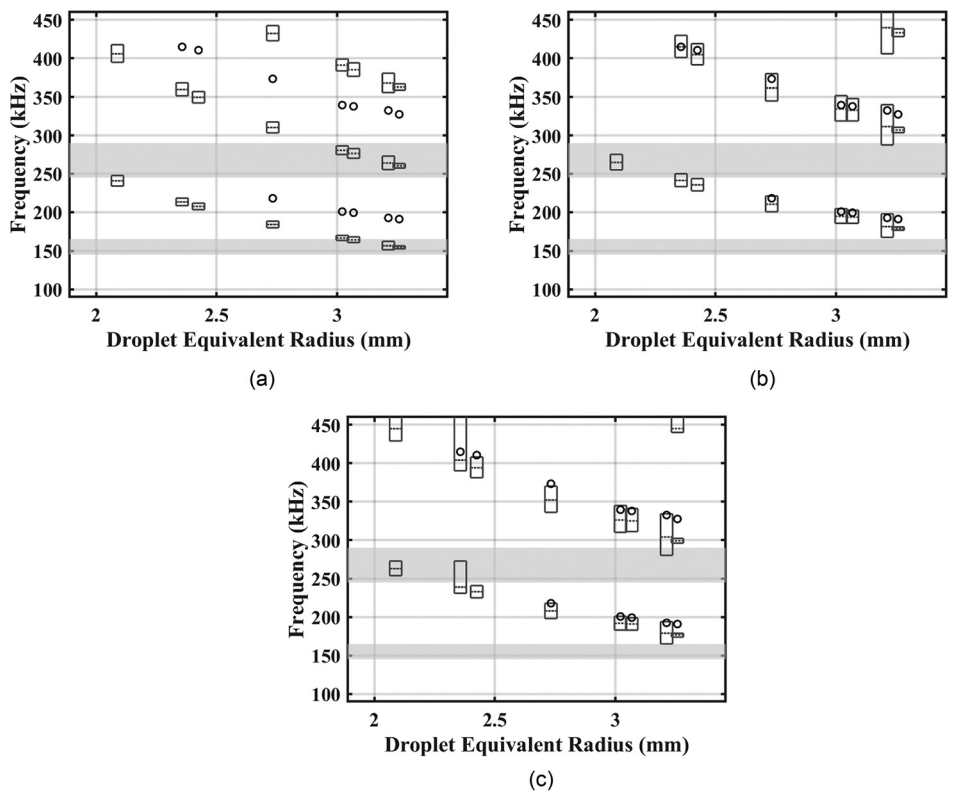

FIG. 11. The frequency of the null for all grouped XIK droplets compared to the modeled null frequency. The gray boxes show the range of the frequency off the null computed at the 95% confidence limits of the droplet size as measured by the imaging system. The dashed gray line in the gray box shows the null frequency for the mean droplet size. The null frequency from the measured backscatter is shown with a black circle. The modeled null frequencies are for (a) Anderson (1950), (b) DWBA, and (c) the BEM. The gray bands indicate the gap in ensonified frequencies between transducers. For recorded data, nulls detected within 10 kHz of the gap in frequencies between transducers are excluded. Note that no nulls were detected for the measured TS of the smallest XIK droplet.

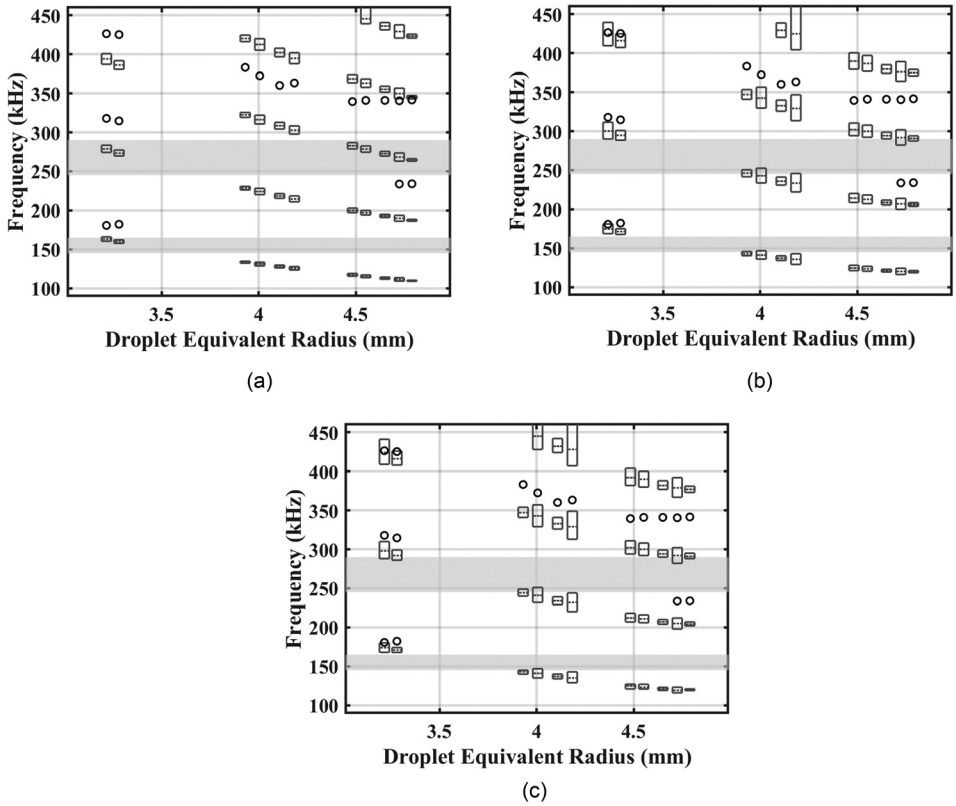

FIG. 12. The frequency of the null for all grouped BAV droplets compared to the modeled null frequency. The gray boxes show the range of the frequency off the null computed at the 95% confidence limits of the droplet size as measured by the imaging system. The dashed gray line in the gray box shows the null frequency for the mean droplet size. The null frequency from the measured backscatter is shown with a black circle. The modeled null frequencies are for (a) Anderson (1950), (b) DWBA, and (c) the BEM. The gray bands indicate the gap in ensonified frequencies between transducers. For recorded data, nulls detected within 10 kHz of the gap in frequencies between transducers are excluded.

droplet is excluded, the RMS error for ANS drops to 15 kHz and 10 kHz for the BEM and DWBA, respectively. The lower RMS error for the DWBA indicated that it is a slightly better predictor of null frequency. The frequency of the nulls for BAV, on the other hand, do not agree with the DWBA or BEM over most of the size range. The RMS error between the measured null frequency and the null predicted was 31 kHz and 32 kHz for the DWBA and BEM, respectively (assuming that the predicted null was always lower in frequency than the measured). The discrepancy between the measured and modeled null frequency increases with increasing droplet size.

To determine the impact of the discrepancy between the frequency of the modeled and measured null, the difference between the measured droplet size and the size of a droplet predicted by each model was determined. Each of the three models was iteratively computed for a range of droplet sizes to determine what droplet size produced nulls at the same frequency as the measured droplet. For example, nulls were measured at 216 kHz and 365 kHz for an ANS droplet with an equivalent radius of 2.68 mm. The Anderson (1950) model predicts nulls at those same frequencies for a droplet of ANS oil for a 2.36 mm equivalent radius droplet. Therefore the difference between the measured and predicted radii is 0.32 mm, and the volume of the observed droplet was 33% larger than the droplet predicted by the Anderson (1950) model.

Following this example, the % difference in the predicted volume was calculated for all droplet groups and all three models (Fig. 13). All models underpredict the measured droplet volume. The volume error for a given oil increases with increasing droplet size and eccentricity. For XIK and ANS, when compared to the DWBA and BEM, the difference between the predicted and measured droplet sizes was often within the 95% confidence limits (Figs. 10–12), therefore, the predictions agreed with the direct measurements within the accuracy of the imaging system.

In modeling the frequency response, it was assumed that the impact of dispersion in sound speed was negligible. The sound speed of all oils was measured at 750 kHz (Loranger *et al.*, 2018), and there is potential for changes to that sound speed at the frequencies in this study due to dispersion. However, the relationship between sound speed (and attenuation) and frequency for all of the oils is not known, and therefore could not be included in the model. BAV produced the largest droplets and had the highest viscosity oil by an order of magnitude and therefore attenuation is likely to be most pronounced in BAV droplets. The offset in the null frequency in BAV between the measurements and both the DWBA and BEM could be the result of such dispersion. The frequency dependence of the sound speed for these oils is an area requiring further research.

VII. CONCLUSIONS

The BEM, DWBA, and Anderson (1950) models are good predictors of the peak of the TS; the RMS difference in backscattering cross section between the observation and models at the peak frequency is equivalent to 1.8 dB, 1.0 dB, and 0.5 dB for Anderson (1950), the DWBA, and BEM, respectively. The DWBA and BEM predict the null frequency for an oblate sphere of ANS and XIK crude oil within the accuracy of the droplet measuring system. BAV, the DWBA, and BEM predict a droplet within 20% of the observed volume for the smallest droplets; however, as

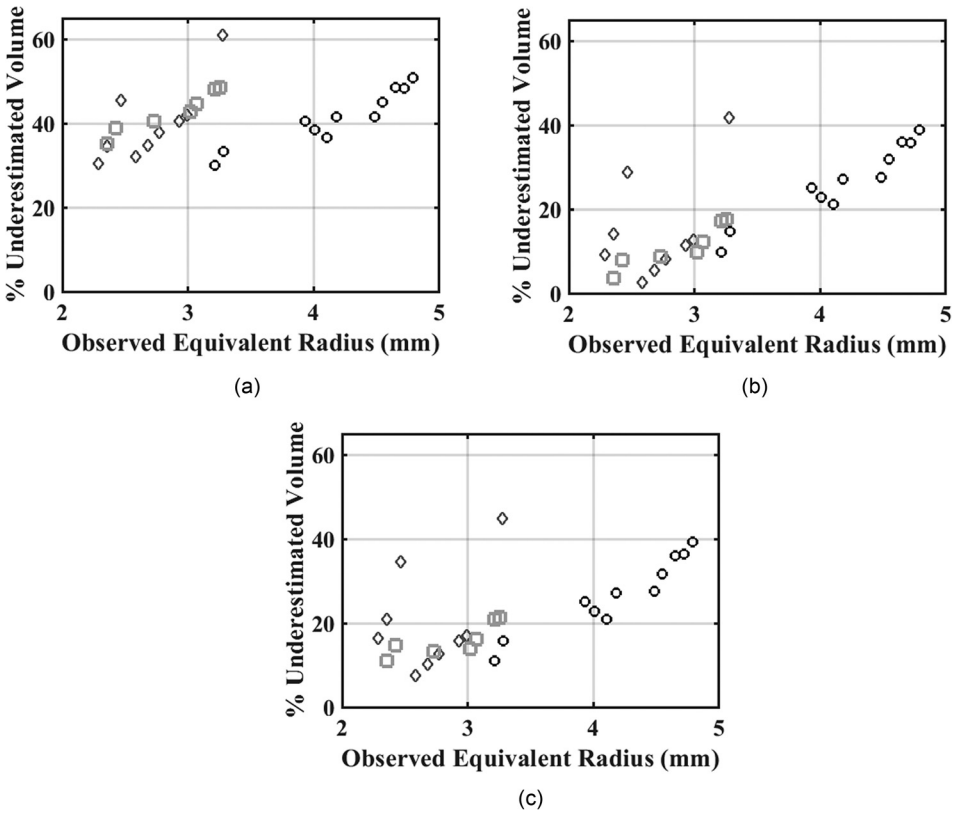

FIG. 13. Percent error in the estimated droplet volume of a droplet when using the null frequency to determine droplet size with (a) Anderson (1950), (b) the DWBA, and (c) the BEM for ANS (dark gray diamonds), XIK (light gray squares), and BAV (black circles).

droplet size increases the DWBA and BEM increasingly underpredict the volume with a maximum underprediction of almost 40% for the largest droplet. The Anderson model tends to underpredict droplet volume by between 30% and 50% with increasing error as droplet size and eccentricity increase for an individual oil.

Inversions of the DWBA and BEM to determine droplet size resulted in agreement between the measured and predicted droplet volume for the lower viscosity oils in this experiment (ANS and XIK). These lower viscosity oils also resulted in smaller oil droplets compared with the higher viscosity oil (BAV). For the higher viscosity oil, BAV, which produced larger droplets, significant errors were observed between the predicted and measured sizes with increasing discrepancy between predicted and measured sizes as droplet size increases. A potential source of this discrepancy is dispersion, which was not accounted for here, and further research on these processes is necessary to determine the impact of dispersion on broadband backscatter from oil droplets.

ACKNOWLEDGMENTS

We acknowledge the Center for Complex Fluids at Carnegie Mellon University for providing the surface tension analysis. We thank Paul Lavoie from UNH for assistance in the design and construction of the droplet making system, Peter Vrolijk and John Blum from Exxon Mobile, and Andone Lavery of Woods Hole Oceanographic Institution for providing crude oil samples. The work was supported by the National Oceanic and Atmospheric Administration (Grant No. NA15NOS4000200).

Alvarez, N. J., Walker, L. M., and Anna, S. L. (**2010**). "A microtensiometer to probe the effect of radius of curvature on surfactant transport to a spherical interface," Langmuir **26**(16), 13310–13319.

Anderson, V. (**1950**). "Sound scattering from a fluid sphere," J. Acoust. Soc. Am. **22**(4), 426–431.

ASTM D7867-13 (**2013**). *Standard Test Methods for Measurement of the Rotational Viscosity of Paints, Inks and Related Liquid Materials as a Function of Temperature* (American Society for Testing and Materials, Philadelphia, PA).

Bilaniuk, N., and Wong, G. S. K. (**1993**). "Speed of sound in pure water as a function of temperature," J. Acoust. Soc. Am. **93**(3), 1609–1612.

Camilli, R., Di Iorio, D., Bowen, A., Reddy, C. M., Techet, A. H., Yoerger, D. R., Whitcomb, L. L., Seewald, J. S., Sylva, S. P., and Fenwick, J. (**2012**). "Acoustic measurement of the Deepwater Horizon Macondo well flow rate," Proc. Natl. Acad. Sci. U.S.A. **109**(50), 20235–20239.

Chu, D., Foote, K. G., and Stanton, T. K. (**1993**). "Further analysis of target strength measurements of Antarctic krill at 38 and 120 kHz: Comparison with deformed cylinder model and inference of orientation distribution," J. Acoust. Soc. Am. **93**(5), 2985–2988.

Clift, R., Grace, J. R., and Weber, M. E. (**1978**). *Bubbles, Drops, and Particles* (Academic, New York, NY), p. 380.

Coombes, K. R., Tsavachidis, S., Morris, J. S., Baggerly, K. A., Hung, M. C., and Kuerer, H. M. (**2005**). "Improved peak detection and quantification of mass spectrometry data acquired from surface-enhanced laser desorption and ionization by denoising spectra with the undecimated discrete wavelet transform," Proteomics **5**(16), 4107–4117.

Costabel, M., and Stephen, E. (**1985**). "A direct boundary integral equation method for transmission problems," J. Math. Anal. Appl. **106**, 367–413.

Demer, D. A., Berger, L., Bernasconi, M., Bethke, E., Boswell, K., Chu, D., Domokos, R., Dunford, A., Fässler, S., Gauthier, S., Hufnagle, L. T., Jech, J. M., Bouffant, N., Lebourges-Dhaussy, A., Lurton, X., Macaulay, G. J., Perrot, Y., Ryan, T., Parker-Stetter, S., Stienessen, S., Weber, T., and Williamson, N. (**2015**). "Calibration of acoustic instruments," ICES Coop. Res. Report No. 326.

Francis, D. T. I., and Foote, K. G. (**2003**). "Depth-dependent target strengths of gadoids by the boundary-element method," J. Acoust. Soc. Am. **114**(6), 3136–3146.

Francois, R. E., and Garrison, G. R. (**1982**). "Sound absorption based on ocean measurements. Part II: Boric acid contribution and equation for total absorption," J. Acoust. Soc. Am. **72**(6), 1879–1890.

Holliday, D. V. (**1972**). "Resonance structure in echoes from schooled pelagic fish," J. Acoust. Soc. Am. **51**(4B), 1322–1332.
Jech, J. M., Horne, J. K., Chu, D., Demer, D. A., Francis, D. T. I., Gorska, N., Jones, B., Lavery, A. C., Stanton, T. K., Macaulay, G. J., Reeder, D. B., and Sawada, K. (**2015**). "Comparisons among ten models of acoustic backscattering used in aquatic ecosystem research," J. Acoust. Soc. Am. **138**(6), 3742–3764.
Jones, B. A., Lavery, A. C., and Stanton, T. K. (**2009**). "Use of the distorted wave Born approximation to predict scattering by inhomogeneous objects: Application to squid," J. Acoust. Soc. Am. **125**(1), 73–88.
Kester, D. R., Duedall, I. W., Connors, D. N., and Pytkowicz, R. M. (**1967**). "Preparation of artificial seawater," Limnol. Oceanogr. **12**(1), 176–179.
Kleinman, R. E., and Martin, P. A. (**1988**). "On single integral equations for the transmission problem of acoustics," SIAM J. Appl. Math. **48**(2), 307–325.
Kristensen, Å., and Dalen, J. (**1986**). "Acoustic estimation of size distribution and abundance of zooplankton," J. Acoust. Soc. Am. **80**(2), 601–611.
Lavery, A. C., Chu, D., and Moum, J. N. (**2010**). "Measurements of acoustic scattering from zooplankton and oceanic microstructure using a broadband echosounder," ICES J. Mar. Sci. **67**(2), 379–394.
Loranger, S., Bassett, C., Cole, J. P., Boyle, B., and Weber, T. C. (**2018**). "Acoustically relevant properties of four crude oils at oceanographic temperatures and pressures," J. Acoust. Soc. Am. **144**(5), 2926–2936.
Medwin, H., and Breitz, N. D. (**1989**). "Ambient and transient bubble spectral densities in quiescent seas and under spilling breakers," J. Geophys. Res. **94**(C9), 12751–12759, https://doi.org/10.1029/JC094iC09p12751.
Morris, J. S., Coombes, K. R., Koomen, J., Baggerly, K. A., and Kobayashi, R. (**2005**). "Feature extraction and quantification for mass spectrometry in biomedical applications using the mean spectrum," Bioinformatics **21**(9), 1764–1775.
Morse, P. M., and Ingard, K. U. (**1968**). *Theoretical Acoustics* (Princeton University Press, Princeton, NJ), Chap. 8.
North, E. W., Adams, E. E., Thessen, A. E., Schlag, Z., He, R., Socolofsky, S. A., Masutani, S. M., and Peckham, S. D. (**2015**). "The influence of droplet size and biodegradation on the transport of subsurface oil droplets during the Deepwater Horizon spill: A model sensitivity study," Environ. Res. Lett. **10**(2), 024016.
Okumura, T., Masuya, T., Takao, Y., and Sawada, K. (**2003**). "Acoustic scattering by an arbitrarily shaped body: An application of the boundary-element method," ICES J. Mar. Sci. **60**(3), 563–570.
Pedersen, G. (**2016**). "Simulation of acoustic backscattering from bubbles and droplets under different shape regimes with implications for underwater detection of leakages using active acoustic sensors," J. Acoust. Soc. Am. **140**(4), 3364.
Śmigaj, W., Betcke, T., Arridge, S., Phillips, J., and Schweiger, M. (**2015**). "Solving boundary integral problems with BEM++," ACM Trans. Math. Softw. **41**(2), 1–40.
Socolofsky, S. A., Adams, E. E., and Sherwood, C. R. (**2011**). "Formation dynamics of subsurface hydrocarbon intrusions following the Deepwater Horizon blowout," Geophys. Res. Lett. **38**(9), L09602.
Stanton, T. K., and Chu, D. (**2000**). "Review and recommendations for the modelling of acoustic scattering by fluid-like elongated zooplankton: Euphausiids and copepods," ICES J. Mar. Sci. **57**(4), 793–807.
Stanton, T. K., Chu, D., Jech, J. M., and Irish, J. D. (**2010**). "New broadband methods for resonance classification and high-resolution imagery of fish with swimbladders using a modified commercial broadband echosounder," ICES J. Mar. Sci. **67**(2), 365–378.
Stanton, T. K., Chu, D., and Wiebe, P. H. (**1998**). "Sound scattering by several zooplankton groups. II. Scattering models," J. Acoust. Soc. Am. **103**(1), 236.
Stanton, T. K., Chu, D., Wiebe, P. H., and Clay, C. S. (**1993**). "Average echoes from randomly oriented random-length finite cylinders: Zooplankton models," J. Acoust. Soc. Am. **94**(6), 3463–3472.
Terrill, E. J., and Melville, W. K. (**2000**). "A broadband acoustic technique for measuring bubble size distributions: Laboratory and shallow water measurements," J. Atmos. Ocean. Technol. **17**(2), 220–240.
Thompson, C. H., and Love, R. H. (**1996**). "Determination of fish size distributions and areal densities using broadband low-frequency measurements," ICES J. Mar. Sci. **53**(2), 197–201.
Vagle, S., and Farmer, D. M. (**1992**). "The measurement of bubble-size distributions by acoustical backscatter," J. Atmos. Ocean. Technol. **9**(5), 630–644.
Weber, T. C., De Robertis, A., Greenaway, S. F., Smith, S., Mayer, L., and Rice, G. (**2012**). "Estimating oil concentration and flow rate with calibrated vessel-mounted acoustic echo sounders.," Proc. Natl. Acad. Sci. U.S.A. **109**(50), 20240–20245.
Weber, T. C., and Ward, L. G. (**2015**). "Observations of backscatter from sand and gravel seafloors between 170 and 250 kHz," J. Acoust. Soc. Am. **138**(4), 2169–2180.
Zhao, L., Boufadel, M. C., Socolofsky, S. A., Adams, E., King, T., and Lee, K. (**2014**). "Evolution of droplets in subsea oil and gas blowouts: Development and validation of the numerical model VDROP-J," Mar. Pollut. Bull. **83**(1), 58–69.